Photoflash and laser ignition of full density nano-aluminum PVDF films

Kyle E. Uhlenhake [a,*], Daniel Olsen [b], Mateo Gomez [a], Metin Örnek [a], Min Zhou [b], Steven F. Son [a,c]

[a] *School of Mechanical Engineering, Purdue University, West Lafayette, IN 47906, United States*
[b] *School of Mechanical Engineering, Georgia Institute of Technology, Atlanta, GA 30313, United States*
[c] *Purdue Energetics Research Center, Purdue University, West Lafayette, IN 47906, United States*

A B S T R A C T

Laser or flash excitation is an attractive ignition option for many energetic systems because of increased safety and control. Commonly used electrical ignition systems are more likely to cause accidental ignition due to stray currents. Upgrading to laser or flash ignition mitigates this problem as well as allowing the ignition at multiple sites more easily for improved control of the energy release. Carbon nanotubes and nanoscale aluminum have been shown to be flash ignitable in loose powders or very porous low-density materials; however, these previous low-density formulations may not be as useful in practical energetic systems. In this study, nano aluminum particles are combined with a polyvinylidene fluoride binder/oxidizer in order to create a full-density photosensitive material. Using a low energy broadband flash source and an Nd:YAG laser at 1064 and 532 nm, films of nano aluminum and polyvinylidene fluoride were successfully ignited experimentally and ignition response was quantified. Solids loading was found to be the dominating factor controlling minimum ignition energies, with the lowest energies observed at 20 to 25 wt.% nAl. Simulations of the wave and particle interactions were modeled with COMSOL Multiphysics® for both the flash and laser-induced heating. The results show that optimal energy absorption occurs at nAl particle fractions of 20–25 wt.%, consistent with the experimental observation. Additionally, the results show the effect of plasmonic resonant enhancement of the heating, specifically at lower wavelengths near 250 nm.

1. Introduction

The ignition of energetic materials, and specifically solid propellants, is a complex process that must be safe, consistent, and precisely controlled. There is a wide range of applications with specific ignition requirements for solid propellants including inflation of airbags, propulsion systems (including rockets), as well as arm and fire devices. Currently, electrical or percussion pyrotechnic igniters are most the commonly used ignition systems. These systems must be carefully designed to deliver the proper amount of energy to a specified surface area of the propellant [1,2]. A photon light source (i.e. flash or laser-based) can potentially be used to ignite energetic materials with lower input energy and more precise spatial and temporal control, thereby improving safety and reliability by eliminating electrical systems used in pyrotechnic igniters.

In addition, they could be potentially safer from stray electrical charges causing unintentional ignition.

Carbon nanotubes, nanoscale aluminum particles (nAl), and nanoscale iron particles (nFe) have been shown to be flash ignitable [3–13]. However, flash ignition of these materials has only been achieved in loose powders or at very low densities. Consequently, these formulations may not be useful in practical energetic systems where density is critical for energetic performance. Laser ignition of solid propellants has been studied extensively [14–30], as well as adding photosensitive particles to improve laser ignition [17,19,29–39]. In general, direct laser ignition of full-density propellants, or other dense materials, requires significant energy, which has made this approach uncommon. Therefore, a photosensitive high-density energetic material would be attractive as it could enable the use of radiative ignition in practical applications at reasonable laser energy levels.

One of the first flash ignitable materials discovered was single-walled carbon nanotubes [3]. Carbon nanotubes could only be flash ignited in dry, non-compacted samples. At higher densities, the en-

* Corresponding author.
  E-mail address: kuhlenh@purdue.edu (K.E. Uhlenhake).

ergy required for ignition rises sharply, which Ajayan et al. [3] attributed to increased heat conduction into the material. Later studies doped low-density pentaerythritol tetranitrate (PETN) with carbon nanotubes to produce a flash ignited reactive wave [4]. This research demonstrated the capability to ignite composite materials, below the theoretical maximum density, with a relatively simple flash ignition setup.

Beyond carbon nanotubes, flash ignition has been studied for a variety of materials. For example, a study using freestanding nano-porous silicon films showed ignition sensitivity depended on the rate of heat loss from the ignition site before decomposition and ignition occurred. Consequently, again, material porosity was important as it led to hotspots where ignition would start [40]. Narendra et al. [19] showed that certain high-nitrogen energetic materials, e.g., 3,6-bis(1H-1,2,3,4-tetrazol-5-amino)-s-tetrazine (BTATz) and 3,3′-azo-bis(6-amino-1,2,4,5-tetrazine) (DAATO3.5) powders were flash ignitable. The study hypothesized that the flash ignition was achieved due to the high absorption of visible light and the reaction dynamics of these high nitrogen materials. These high-nitrogen materials were also ignited with a CO_2 laser at a wavelength of 10.6 µm at a fraction of the energy required for photoflash [19]. Overall, these studies were limited to less desirable, lower-density materials but demonstrated the capability for direct flash ignition of energetic materials.

Tseng et al. showed that nanotube photo-sensitivity was likely due to catalyst particles, such as nano-iron particles left behind from the synthesis process [6]. Since then, flash ignition has been further studied for both nano-aluminum (nAl) and nano-iron (nFe) particles [6–11]. Flash ignition of nAl has been of specific interest due to aluminum's widespread use in energetic materials. Flash ignition is heavily dependent on the size of the particles, as micron-aluminum will not flash ignite [7]. This is likely due to nAl having lower ignition temperatures than micron-aluminum, as well as being absorption dominated rather than scattering dominated at the nanoscale [7,8]. While some micron-sized particles have been shown to be optically sensitive, they require either mechanical activation or a photosensitive additive such as graphene oxide or tungsten oxide nanoparticles [12,41,42]. Ohkura et al. [7] concluded that the particles needed to be submicron in diameter and that packing density played a critical role in flash ignition. As packing density was increased, the temperature achieved from a flash was modeled to rise due to an increased density of absorbing nAl particles. However, packing densities above 50% by volume aluminum in air were not considered.

Modeling of the optical ignition for aluminum is also of interest in order to better understand the mechanisms behind ignition and predict the ideal circumstances for viable optical ignition. Jin et al. [33] developed a model for laser ignition of aluminum particles of different sizes that accounted for the effects of oxide shell thickness, porosity, and combustion characteristics. Other models have focused on plasmonic effects as the main contributor to nAl's optical sensitivity [9,10,43]. Localized surface plasmon resonance is the resonant oscillation of free electrons in the metals that can confine or enhance the radiation energy absorbed from light sources. These effects are specifically prominent in nanostructures smaller than the light wavelengths interacting with them, and multiple studies have shown aluminum nanoparticles to exhibit these interactions [9,10,43,44].

Flash ignition of nAl becomes difficult at higher densities because the energy threshold for ignition increases dramatically with higher densities [3,18,41]. Sippel et al. [41] investigated the use of micron aluminum combined with fluoropolymer polycarbon monofluoride (PMF) using mechanical activation (low and high energy milling) to form nanoscale inclusions of PMF in the aluminum. These particles had high aluminum content (70 and 90 wt.%) and were also found to flash ignite similarly to nAl parti-

cles. However, only the low energy milled particles pressed to 50% theoretical maximum density (TMD) or less could flash be ignited. Higher TMD pellets were no longer flash ignitable, likely due to increased thermal diffusivity that lowered the temperature achieved from the flash [41].

Extensive research has also been performed on the ignition of solid propellants or explosives using a CO_2 laser (10.6 µm) that is absorbed well by many materials [15–18,24,26–30], but still a relatively high energy pulse is needed for ignition in most cases. Other lasers of interest operate at shorter wavelengths and have been considered also. For example, 1064, 808, and 500 nm lasers have been used to successfully ignited some energetic materials [16,20–22,27]. The ignition energy threshold for these shorter wavelengths was sometimes lower than for CO_2 lasers, but can still be relatively high, and more research is needed to achieve low energy ignition.

In this study, nAl was combined with the fluoropolymer polyvinylidene fluoride (PVDF) to create a high-density, photosensitive energetic material. The objectives of this study were to (i) create a high-density, photosensitive material, that is easily ignited (either laser or a broadband light energy source), and (ii) model nAl/PVDF ignition to determine the critical ignition mechanisms.

2. Materials and methods

2.1. Preparation and microstructural characterization of nAl/PVDF films

Two-gram (2 g) batches of nAl/PVDF mixtures were prepared using nAl particles (80 nm diameter, 70% active content, Novacentrix) and PVDF (Kynar 711, Arkema). The active content of the aluminum was confirmed to be 70 wt.% by fully oxidizing small amounts of nAl particles during thermogravimetric analysis (TGA), and then the percentage of mass gained was used to calculate the percentage of aluminum that transitioned to aluminum oxide. To prevent oxidation, the nAl particles were stored in an argon glove box and only used for the mixing process immediately after they are taken out of the glove box. The nAl was mixed with a solution of dimethylformamide (DMF) at a ratio of 1 g PVDF to 6 mL of DMF. This solution was mixed further using an ultrasonic mixer (Branson Digital Sonifier) for 1.5 min on, 1.5 min off for a total of 3 min on at the amplitude of 15%. PVDF was then added and the mixture was once again sonicated for 1.5 min on, 1.5 min off, for a total of 3 mins on. Once the samples were well mixed, they were cast onto glass slides using a tape caster (MIT Corporation MSK-AFA-HC100) with a heated bed. Films were cast on a heated bed temperature of 125 °C after determining this was the temperature that would ensure high-density films. All films were dried on the heated bed for 15 min and then removed to dry overnight at room temperature. To prevent oxidation of the nAl in the composite, the films were tested within 24 h of being cast, however, the films can be stored in an argon environment to extend the longevity of the nAl/PVDF composites. The film thicknesses were measured with a micrometer to be 35.8 ± 2.6 µm and were then cut into 1 cm² square samples to be used for flash and laser tests.

The films were made with 5, 10, 15, 20, 25, 30, and 40 wt.% nAl content to show the effect of nAl solids loading on the ignition characteristics, with 20 wt.% nAl being stoichiometric. The maximum solids loading was found to be 40 wt.% nAl. Due to nAl's large oxide shell relative to the volume of aluminum, only the active content of aluminum included was used for weight percentage calculations. The active content for the nAl used was confirmed to be 70% using differential scanning calorimetry (DSC) (SDT Q600, TA Instruments).

To study the microstructure of the samples, portions of the nAl/PVDF films were shattered below the PVDF glass transition temperature (−30 °C) in liquid nitrogen, which resulted in smooth
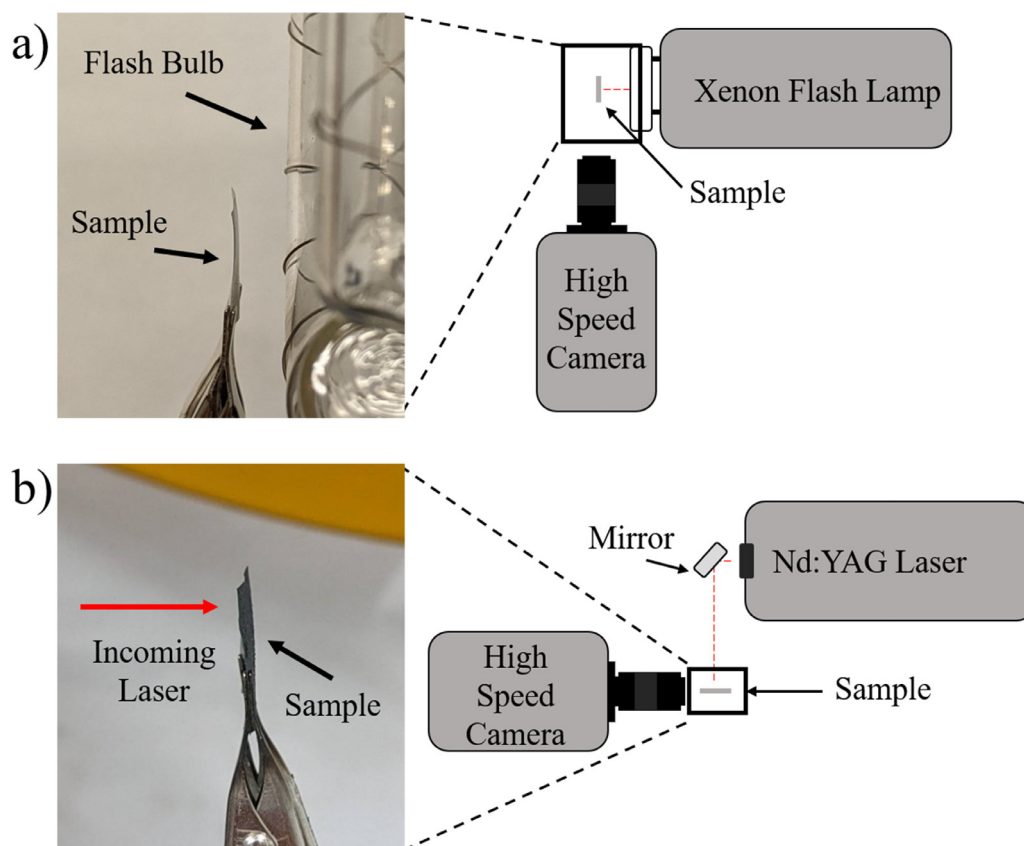
Fig. 1. The schematics of experimental setups for photoflash and laser ignition tests. **a)** Photoflash experimental set up, where sample is held in front of the flash and the energy is controlled by varying distance to the bulb. **b)** Laser ignition set up. For both tests, the absorbing face is in the same plane of the flash bulb and lasers while the camera records from the side.

cross-section surfaces per reference [45]. The shattered films were then mounted on Al stubs and coated with 20 nm palladium layer using a sputter coater (Cressington, UK). Sample morphology and microstructure were investigated using a scanning electron microscope (FEI Nova nanoSEM, Oregon) at an accelerating voltage of 5 kV. The density of the samples was determined using Archimedes' principle.

2.2. Flash and laser ignition tests

Flash ignition tests were carried out using a xenon flash lamp (White Lightning X3200, Paul C. Buff Inc.). The energy output of the xenon flash lamp was measured using a power meter (Gentec) with a 1 cm^2 area open to the flash. The energy fluence was recorded at numerous distances from the flash lamp in order to control the energy deposited into the sample. Samples of nAl/PVDF films were ignited using the flash lamp at specified distances to determine the minimum ignition energy (MIE) using the configuration as shown in Fig. 1. The samples are held in front of the flash bulb by means of a small clip. Multiple configurations were tested to ensure the sample was well fixed and a consistent area was exposed to the flash or laser energy. There was no significant change in MIE regardless of how the samples were secured. The burning samples of films and propellant were recorded using a high-speed video camera (Vision Research, Phantom v10) at 4700 fps. Additionally, the burn rate of the films was captured by using a photodiode (Gentec) to measure light emitted from the burning samples. The photodiode data was then used to measure the ignition delay by calculating the time between the flash being triggered and the initial combustion of the films. After the flash signal was subtracted, the photodiode data first showed a rising slope while the

sample transitioned into steady combustion and then quickly transitioned into a falling slope as the sample burned to completion (an example such a profile can be seen in Supplementary Fig. 1). The onset of ignition was defined to be at the point on the rising slope that is 50% of the peak photodiode output.

For the laser studies, a custom burst-mode Nd:YAG laser was used [46]. For all laser ignition tests, the laser was fired using a pulse burst profile with a 5 ms burst and a repetition rate of 100 kHz at a wavelength of 1064 nm, and 532 nm with an identical burst profile. These burst settings were chosen to closely replicate the flash profile for ignition purposes. Similar to the flash tests, a high-speed camera along with a photodiode was used to capture ignition and the burning rate of the films. The laser was blocked with OD 7 filters corresponding to each wavelength used. To study the effect of heating rates, the laser profile was adjusted to simulate more commercially common lasers such as Q-switched and continuous-wave lasers. For these studies, the laser produced a 2.0 ms and a 0.2 ms burst at 5 MHz with 10 ns pulses to approximate a continuous wave and a Q-switched laser, respectively. The profiles of these laser bursts and pulses can be seen in the supplementary materials (Supplementary Fig. 2).

Due to the latent distribution nature of nAl/PVDF when flash and laser ignition testing, the Neyer's sensitivity test [47] was utilized to determine MIE values. For all sensitivity tests, a significant number of samples ($n > 30$) were taken according to the Neyer sensitivity test. The test then utilized maximum likelihood estimations to determine the next test point and the final MIE [47]. Samples were taken until the Neyer's test displayed the average and standard deviation showed independence and a confidence interval could be determined for the tests. The energy fluence where ignition was observed is defined herein as the ignition energy and

is the value at which the sample is expected to ignite 50% of the time; this is presented along with the 95% confidence interval for all cases.

2.3. Modeling/Simulations

Along with the experimental studies, computational analyses of the laser and flash heating of the nAl/PVDF propellants were carried out. The primary intent is to (i) understand how heating occurs through the interactions of the electric and magnetic fields (E-field and M-field respectively) of the incident radiation with the composite microstructures of both dielectric and conducting constituents and (ii) delineate the trends in heating that leads to ignition. To this end, the microstructure models include three constituents: PVDF, aluminum oxide (Al_2O_3), and aluminum (Al). Particles in the microstructure have an 80 nm diameter consisting of an Al core with a 3 nm Al_2O_3 shell. This oxide shell thickness matches the oxide shell thickness for the nAl used experimentally at 70 wt.% active aluminum. The core-shell structured particles (Supplementary Fig 3.) are embedded in the PVDF binder matrix. Microstructures with four solids loading levels are considered. These microstructures were used in electrodynamic calculations which track the e-fields and the m-fields through which dielectric heating and conductive heating are evaluated.

The calculations were carried out in COMSOL Multiphysics® [48]. The microstructure samples are 5 μm × 5 μm in size. This size is smaller than the 1 cm × 1 cm × 30 μm sample size used in the experiments, as necessitated by high computational costs for larger samples. Even so, the model allows the mechanisms and extent of heating to be analyzed. This computationally efficient model probes the scattering and adsorption of the incident energy by the particles and the binder in microstructures with different solids loadings.

To match the experimental tests, the nAl/PVDF composite microstructures have solids loadings ranging from 10 to 40 wt.% in 5 wt.% increments. For each solids loading level, five statistically equivalent microstructure sample sets (SEMSS) were generated. The images of four representative samples are shown in Supplementary Fig. 4, one from each of the SEMSS at four solids loading levels. The oxide shell thickness is chosen to match the 70% active aluminum content found for the nAl powders used in the experiments. The particles are approximately uniformly distributed; particulate agglomeration and voids were not modeled. SEM images of the films showed a random distribution of nAl particles in the PVDF matrix. Therefore, a random distribution of nAl particles was selected for the modeling study as well. While such images can be digitized and used in the simulations in the future, the computational design approach of microstructures taken here has the benefit of allowing systematic variations of microstructure attributes that are practically difficult to achieve in experiments. The ignition/excitation condition emulates that in the experiments in Fig. 2, with the incident wave coming from the top of the two-dimensional sample and the E-field vector in plane and horizontal, as illustrated in Fig. 2. The boundary condition at the bottom edge of the sample was transparent.

Modeling is based on a commonly used framework for particles of this size. The input optical excitation is that from the experiments and is specified by defining the incident electric field. All material properties used are taken from reports from experiments in the literature. The electrodynamic governing equation concerning the conservation of electric charge in the frequency domain has the form of

$$\nabla \times \mu_r^{-1} (\nabla \times \mathbf{E}) - k^2 \left(\varepsilon_r - \frac{j\sigma}{\omega \varepsilon_0} \right) \mathbf{E} = 0, \tag{1}$$
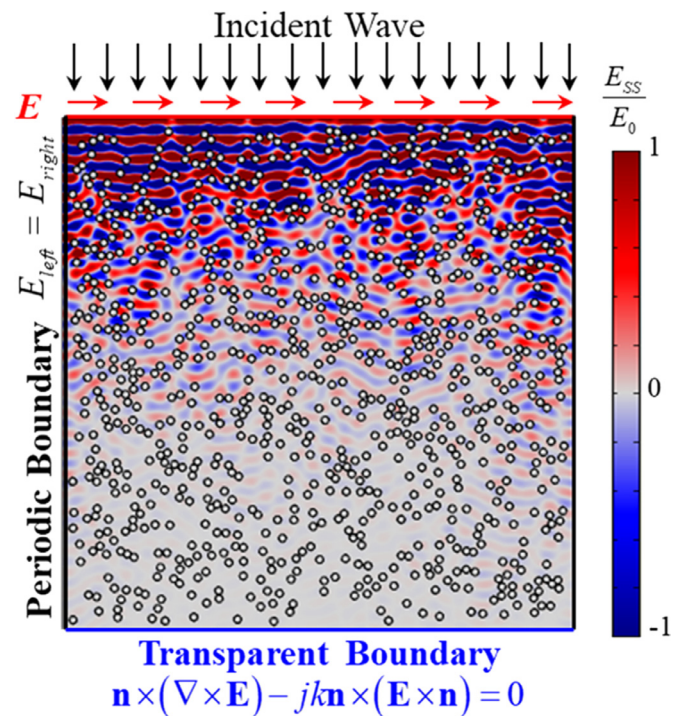
Fig. 2. Configuration of the computational model using a 5 μm × 5 μm microstructure sample. The transparent boundary at the bottom allows the waves to pass through without reflection back into the domain. The lateral boundaries are periodic.

where, $\mathbf{E}$ is the electric field vector, $\nabla \times$ is the curl operator, μ_r is real permeability, k is the wavenumber, ε_r is permittivity, σ is electrical conductivity, $j = \sqrt{-1}$ is the imaginary unit, ε_0 is the vacuum permittivity, and ω is frequency. The transparent boundary condition at the bottom edge of the sample is

$$\mathbf{n} \times (\nabla \times \mathbf{E}) - jk\mathbf{n} \times (\mathbf{E} \times \mathbf{n}) = 0, \tag{2}$$

where, $\mathbf{n}$ is unit normal to the boundary surface. Since heat generation and conduction are considered, the governing equation relates to the time-dependent conservation of energy in the form of

$$\rho C_p \frac{\partial T}{\partial t} + \kappa \nabla^2 T = q, \tag{3}$$

where, ρ is the mass density, C_p is the specific heat under constant pressure, T is temperature, κ is thermal conductivity, and q is the heat generation rate per unit volume due to conductive and dielectric dissipation, i.e.,

$$q = \frac{1}{2} \sigma |\mathbf{E}|^2 + \frac{1}{2} \omega \varepsilon_0 \varepsilon'' |\mathbf{E}|^2 \tag{4}$$

where, ε'' is the imaginary part of the complex permittivity. The first term represents conductive joule heating or the power, and the second term is for dielectric heating. The heat generation rate can be used to obtain the accumulative heat deposited Q in a volume V of a sample up to a time t via

$$Q = \int_0^t \int_V q \, dV \, dt. \tag{5}$$

This quantity will be used later to assess the heating in different material cases.

To assess the amount of energy reflected and transmitted, the energy at both the top and bottom surfaces. The energy at each surface and an understanding of the applied energy allows for the reflection and transmission coefficients for the material to be cal-

culated [49].

$$S_R = \frac{\int_{S1} (\mathbf{E}_c - \mathbf{E}_1) \cdot \mathbf{E}_1 \, dS}{\int_{S1} \mathbf{E}_1 \cdot \mathbf{E}_1 \, dS} = \sqrt{\frac{\text{Reflected Energy}}{\text{Total Energy}}} \qquad (6)$$

where, S_R is the reflected energy, $\mathbf{E}_c$ is the calculated electric field at a surface, and $\mathbf{E}_1$ is the expected electric field mode at the top surface.

$$S_T = \frac{\int_{S2} \mathbf{E}_c \cdot \mathbf{E}_2 \, dS}{\int_{S2} \mathbf{E}_2 \cdot \mathbf{E}_2 \, dS} = \sqrt{\frac{\text{Transmitted Energy}}{\text{Total Energy}}} \qquad (7)$$

where, S_T is the transmitted energy and $\mathbf{E}_2$ is the expected electric field mode at the top surface.

The experimentally measured spectrum of the xenon flash was used to calculate the heating through superposition of calculations at discrete single wavelengths from 200 to 1000 nm. The integration accounts for the relative intensities of different wavelengths in the xenon flash pulse over the flash duration [50,51]. Laser heating at 1064 nm, 532 nm, and 250 nm wavelengths were considered. The 250 nm wavelength was chosen to isolate the possible effect of plasmon resonance associated with the nAl particles. This wavelength is similar to the wavelengths studied by Chong et al. [9]. This effect will be described in more detail later.

The simulations of the material response to YAG laser excitation follow two steps. First, the E-field history in the microstructure is evaluated using Eq. (1) along with the period boundary condition (Fig. 2) and transparent boundary condition in Eq. (2). The resulting heating rate is calculated using Eq. (4) [52]. Subsequently, the temperature field is obtained by solving Eq. (3) The laser excitation is accounted for by specifying the E-field at the top edge of the microstructure in Fig. 2 over the duration of desired exposure. Although calculations are carried out for shorter durations than those in the experiments, they are long enough to allow the heating mechanisms and trends to be analyzed. The simulations are inert and focus on how energy deposition is affected by the microstructure and solids loading in order to understand the trends observed in the experiments. While exothermic chemical reactions are a critical aspect of the combustion process for the nAl/PVDF films, the focus of this paper is to understand the heating mechanisms and the conversion of electromagnetic energy into heat energy for samples with various solids loading. The goal is to understand the conditions most conducive to maximum energy absorption and heating so as to enhance the sensitivity of nAl/PVDF to optical ignition. In contrast, the effects of chemistry and pre-ignition reactions on nAl/PVDF combustion are more of interest in a future publication.

Because the electromagnetic wave traverses the microstructure on an order of picoseconds, the E-field in the microstructure is obtained by solving Eq. (1) in the frequency domain at each point of time in a time-independent manner with the prescribed boundary condition. The time increment in this process is 1 ps. Due to the vastly disparate time scales of the EM and thermal conduction processes, the heat equation Eq. (3) is solved independently with a much longer time step of 3 ns, with the heat generation rate q being evaluated via Eq. (4) using the result of the EM solution process. This small time-step is sufficient to resolve the laser pulse duration of 10 ns. This solution procedure is frequently used and is available in COMSOL. One benefit of this procedure is that it is computationally more efficient and offers sufficiently accurate results. Due to the lack of experimental data, the time-dependence of material properties is not considered.

The smallest constituent is the nAl particles which have a radius of 35 nm. COMSOL Multiphysics® was used to generate mesh with triangular elements. The element size is 5 nm, allowing for ~14 elements across each particle. A mesh convergence study is carried out, showing that the difference in the electric field for the shortest wavelength of 250 nm using element sizes of 5 nm and

Table 1
The measured densities of nAl/PVDF films using Archimedes' principle and calculated TMD's as a function of solids loading.

Solids Loading of nAl in PVDF	Density (g/cm³)	Theoretical Max Density (% TMD)
10%	1.84	97.9 ± 0.9
15%	1.88	97.3 ± 1.2
20%	1.96	98.2 ± 0.6
25%	2.00	97.9 ± 1.0
30%	2.03	96.4 ± 1.4
40%	1.97	88.9 ± 0.8

2 nm is less than 1%. Therefore, the chosen element size provides sufficient accuracy. In order to make sure that the temperature rise and heating effects are accurately captured, several time steps of less than 10 ns are used. The results show that the difference in temperature between the time steps of 5 ns and 3 ns is ~2%. Therefore, all calculations are carried out using the time step of 3 ns.

3. Results and discussion

3.1. Microstructural characterization

The porosity of the films is controlled by the temperature of the tape caster bed during casting. By increasing the temperature of the drying bed, DMF is allowed to evaporate out rapidly from the liquid mixture of nAl/PVDF, resulting in high-density thin films being formed. This effect can be seen in Fig. 3, where cross-section images of the films cast at a range of temperatures are shown. At temperatures up to 65 °C, large macroscopic porosities can be observed. The porosity in the films is decreased when the heated tape casting bed temperature is increased to 85 °C and is almost completely removed at 105 °C. At 105 °C, the film is generally full density, but defects can occasionally be seen. A casting temperature of 125 °C consistently yields no macroscopic porosity in the film and is considered as the optimum temperature for making full density samples. At this temperature, only defects from snapping the films(out-of-plane features in Fig. 3d) were consistently seen under SEM imaging. The density of 20 wt.% nAl/PVDF processed at 125 °C was quantitatively measured to be 1.96 g/cm² (98.2% TMD) using Archimedes' principle.

To understand the effect of solids loading on structure, SEM imaging was performed on films at both the micro and nano scales with the various solid loadings analyzed. Cross-section SEM micrographs taken from the nAl-PVDF films show that nAl particles were successfully dispersed in the PVDF matrix (Fig. 4). All films were processed at 125 °C in order to ensure they were at the maximum possible density. Low and high magnification images of nAl/PVDF films with a stoichiometric ratio of 20, 30, and 40 wt.% nAl are shown in Fig. 4. The lower magnification shows that the solid film exhibits little to no porosity on a micron scale until 40 wt.% nAl, whereas the high magnification shows that the individual 80 nm aluminum particles are well-dispersed in the PVDF matrix at 20 and 30 wt.% nAl. At 40 wt.% nAl, agglomeration becomes significant. Below 40 wt.% nAl, it is apparent that the nAl is successfully separated, and the PVDF acts as a continuous binder making it a high-density material ideal for photosensitive energetic applications. The critical solids loading limit between 30 and 40 wt.% nAl is due to the high specific surface area of nAl; as the solids loading increases, there is not enough binder to fully wet the surface area of the nAl particles. The density of films at all solids loadings were measured using Archimedes' principle and can be seen in Table 1.
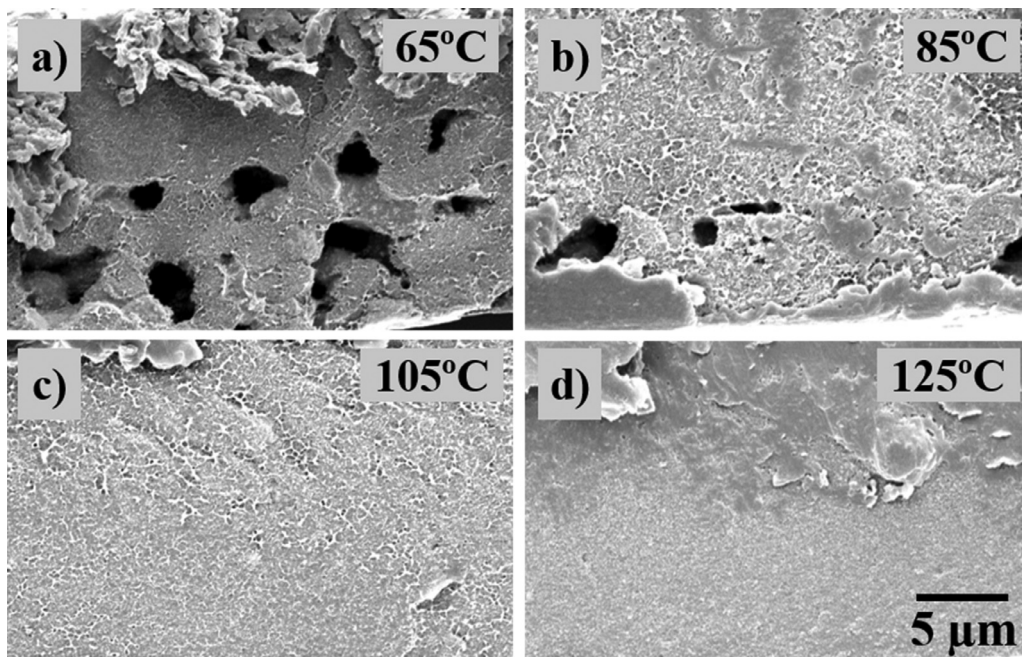
Fig. 3. Cross-section SEM images of 20 wt.% nAl/PVDF films that were tape casted and held at **a)** 65 °C, **b)** 85 °C, **c)** 105 °C, and **d)** 125 °C for 15 mins before being removed and dried at room temperature overnight.
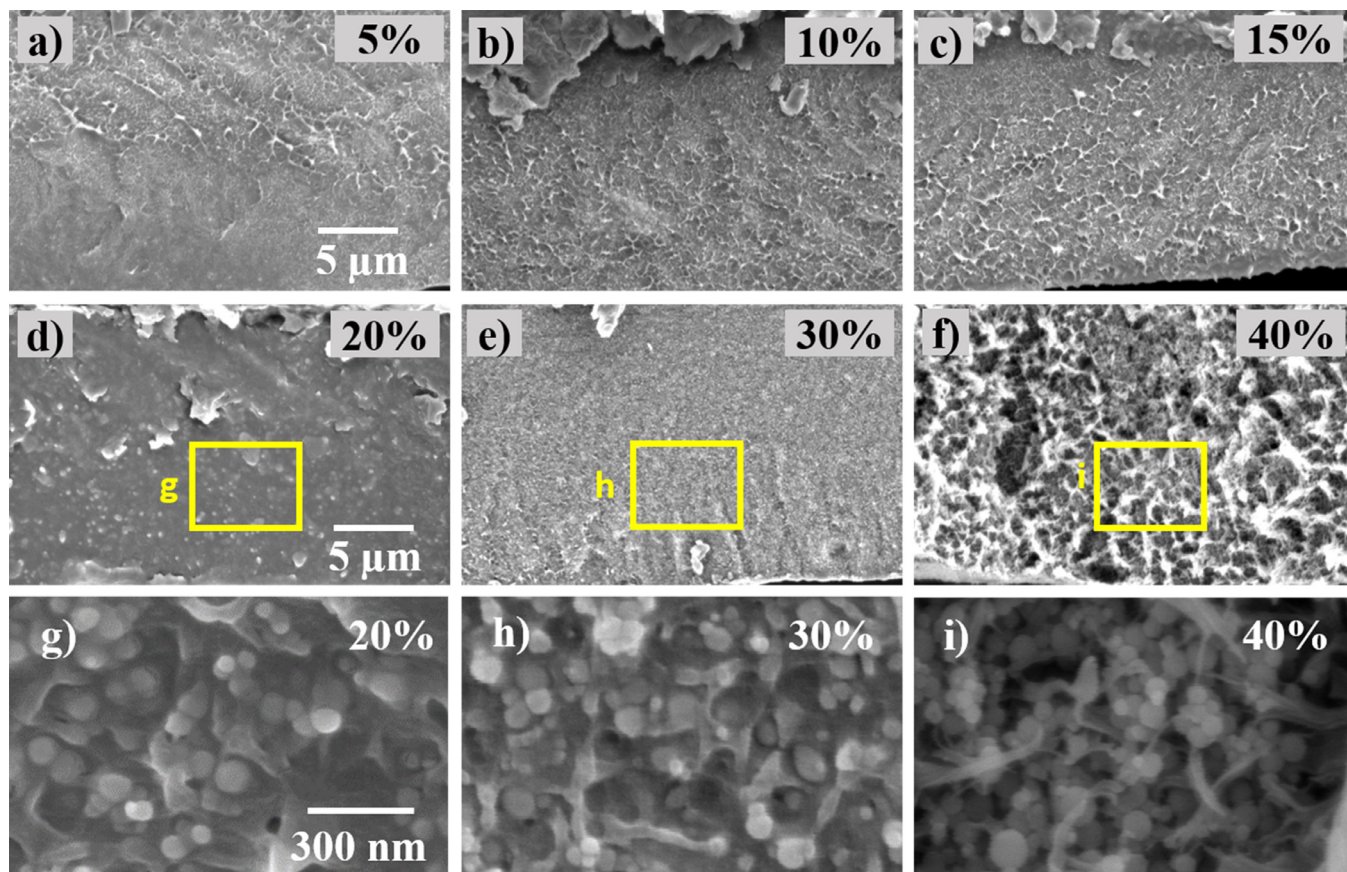
Fig. 4. Cross-sectional low-magnification SEM images of nAl/PVDF films at nAl solids loading of **a)** 5, **b)** 10, **c)** 15, **d)** 20, **e)** 30, and **f)** 40 wt.%. The corresponding higher magnification images of 20, 30 and 40 wt.% nAl images taken from the marked areas in D-f) are shown in g-i). Similar snapping defects as Fig. 3. are observed.
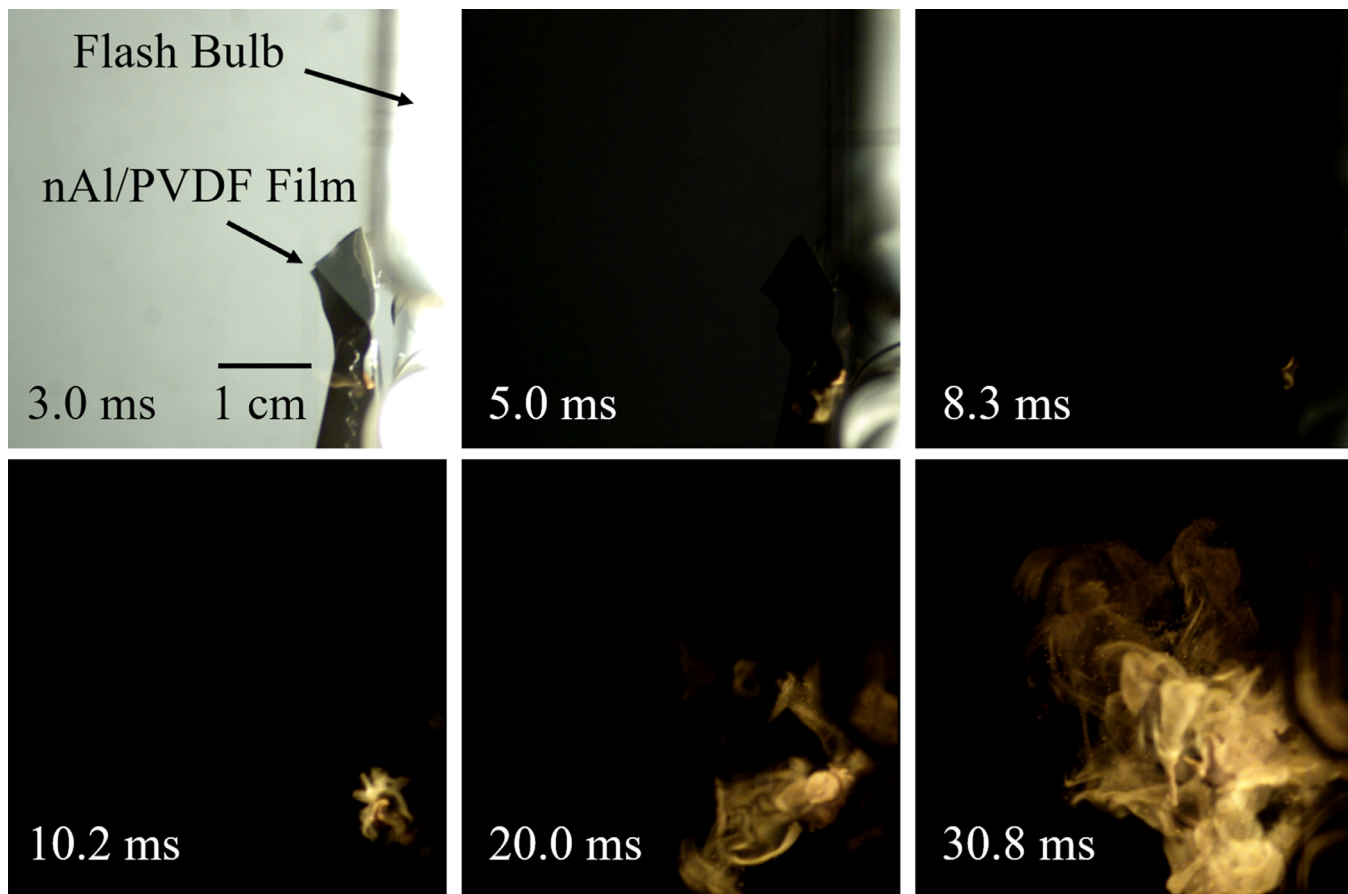
Fig. 5. High speed images of 20 wt.% nAl/PVDF film processed at 125 °C burning from flash ignition. The sample is loaded in front of the flash bulb with the absorbing face exposed to the bulb. The time is measured from the start of the flash. Curling of the sample is due to thermal stress from the sample absorbing the flash energy and converting it to heat. The method of securing the sample had no significant effect on ignition.
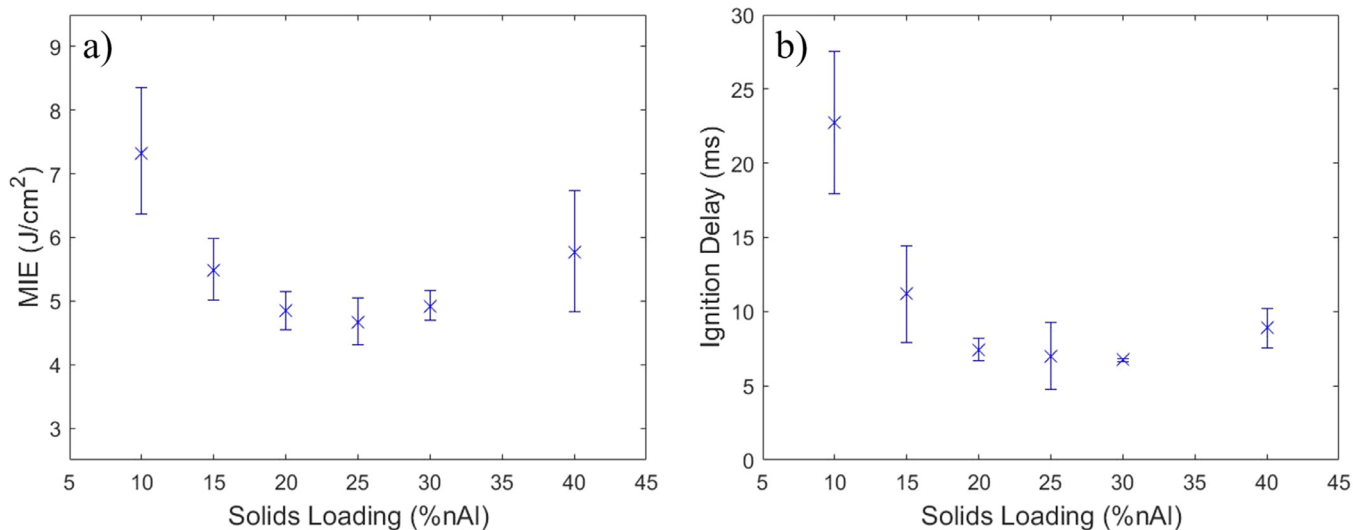
Fig. 6. Flash ignition studies for nAl/PVDF films **a)** Minimum Ignition Energy (MIE) for flash ignition of nAl/PVDF films processed at 125 °C as a function of solids loadings. The blue "x" demonstrates average energy needed to ignite a sample with a 50% likelihood of ignition in the sample at that energy and the bars show the 95% confidence interval for the samples. **b)** Ignition delay along with error bars for samples measured from flash ignition tests using a photodiode at an energy of 8.0 J/cm^2. Ignition was considered constant when the value of the photodiode reached 30% of the maximum after filtering out the light from the flash.
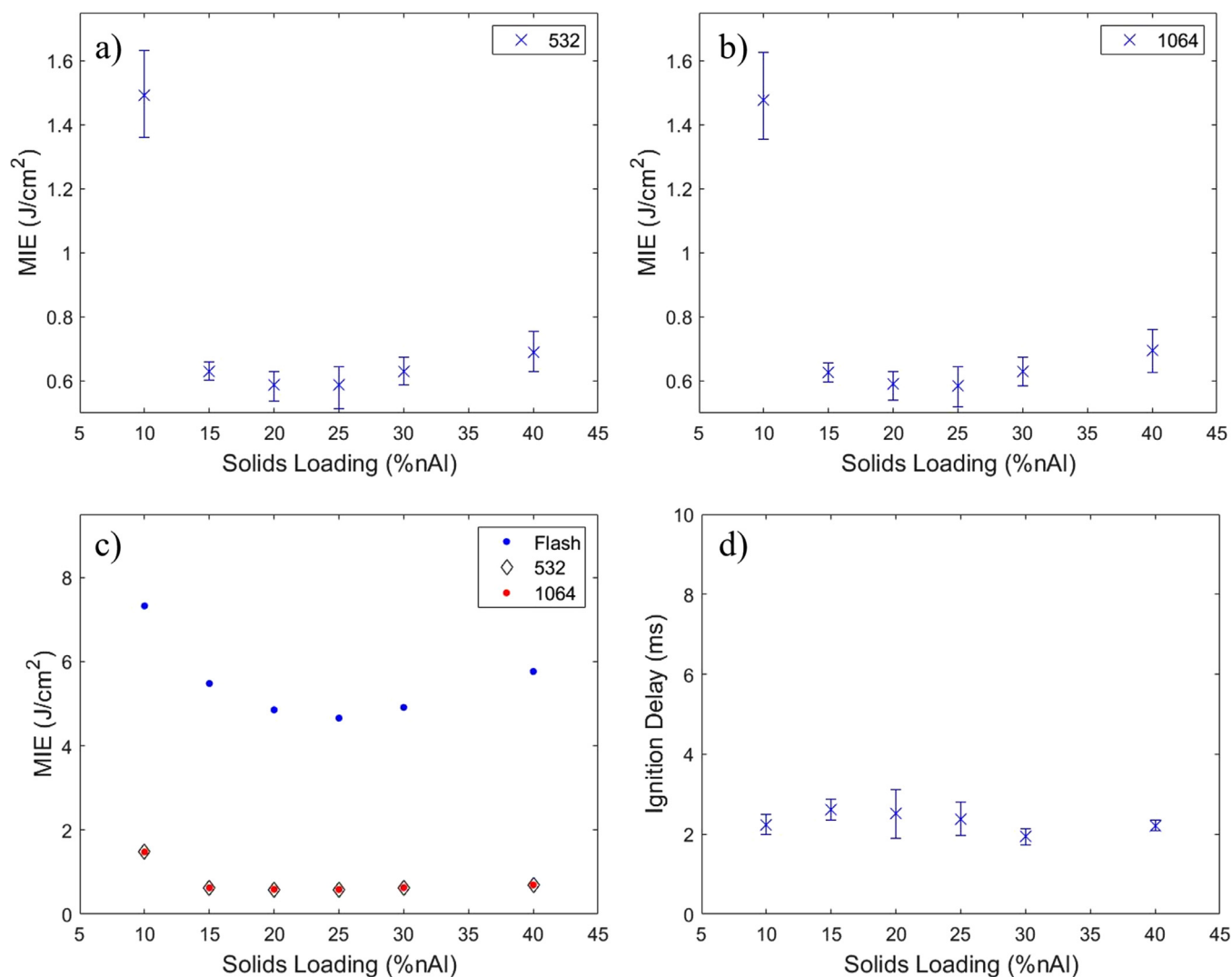
Fig. 7. Laser ignition studies for nAl/PVDF films processed at 125 °C as a function of solids loadings. **a)** MIE for Nd:YAG laser at 532 nm wavelength. **b)** MIE for Nd:YAG laser at 1064 nm wavelength. **c)** A comparison of MIE for samples when flash ignited, and laser ignited at both 1064 and 532 nm wavelengths. **d)** Ignition delay and error bars for nAl/PVDF samples at a wavelength of 1064 nm and an energy of 8.0 J/cm².

3.2. Flash ignition and burning study

High-speed imaging is used to quantify the combustion of nAl/PVDF films after being flash ignited (Fig. 5). As the flash is triggered (3 ms), the nAl/PVDF film absorbs the light energy and the film starts to curl from thermal stresses due to the elastic nature of PVDF. When the film absorbs a critical amount of energy from the flash, a hot spot is formed on the film, which quickly develops into a small flame. This small flame grows slowly, and there is a delay of around 10 ms until full deflagration is seen. The steady burn after the flash consumes the entire sample, confirming that high-density nAl/PVDF materials are sensitive enough to be ignited from a broadband flash.

Flash ignition of nAl/PVDF samples at various solids loadings were characterized by ignition delay and MIE. For samples under 10 wt.% nAl, no flash ignition was observed (Fig. 6), and we speculate that two effects may be causing this; (i) there is not enough nAl in the material to absorb the light energy and the ignition temperature is not reached, or (ii) the nAl near the surface of the sample absorbs enough energy to react with the PVDF binder, but the reaction is quenched due to the surrounding binder acting as a heat sink. However, even at low solids loadings, the absorptivity

of the nAl was still causing the sample to heat up enough to see curling of the films. Additionally, a white powder/residue on the film surfaces, could sometimes be seen by samples with less than 10 wt.% nAl. This is attributed to some of the nAl oxidizing into aluminum oxide.

The MIE values for the nAl/PVDF samples can be seen in Fig. 6. At 10 wt.% nAl, the MIE is significantly higher, and also has a significantly higher confidence interval. The MIE decreases to a minimum near stoichiometric conditions just above 20 wt.% nAl, before rising once again at 40 wt.% nAl. This minimum value near 20 wt.% nAl and subsequent rise as the solids loading is increased can be attributed to the thermal diffusivity of the samples. As more nAl particles are introduced, more of the flash can be absorbed and converted into heat energy. However, as the solids loading is increased, the nAl particles increase the overall thermal diffusivity of the composite, resulting in heat dissipation of the absorbed energy.

Aluminum has a thermal diffusivity of 9.7×10^{-5} m²/s compared to PVDF's 7.2×10^{-8} m²/s, and as a result the composite thermal diffusivity at 10 wt.% nAl can be estimated to be around 1.0×10^{-5} m²/s when assuming a linear model. This value increases to 2.1×10^{-5} m²/s and then 3.1×10^{-5} m²/s at 25 wt.%
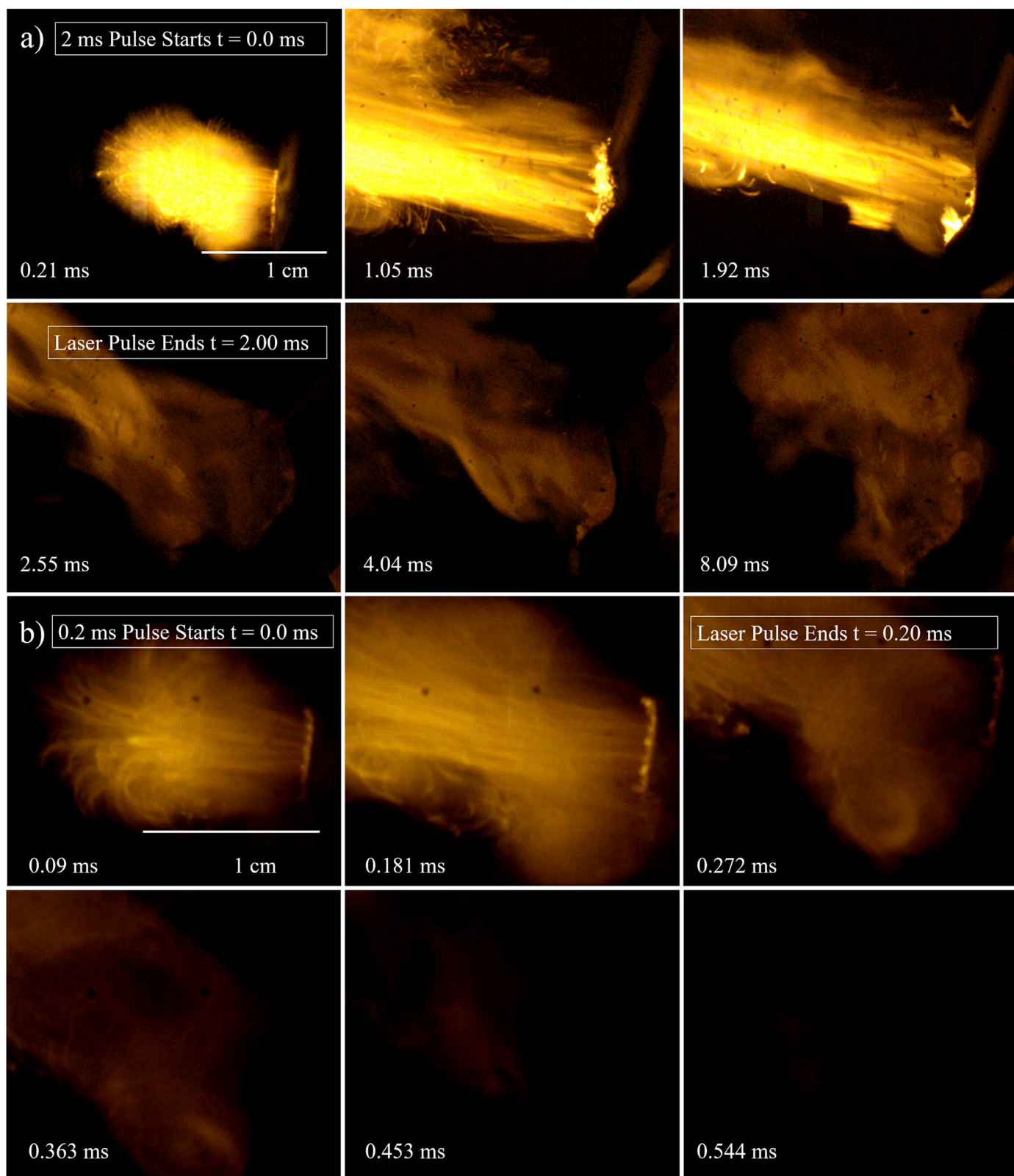
Fig. 8. 1064 nm laser ignition for single pulse. **a)** Continuous wave setting with a 2 ms pulse, where full deflagration of the film can be seen. **b)** Q-switched setting with a 0.2 ms pulse, where the film burns for the duration of the pulse then quickly extinguishes.
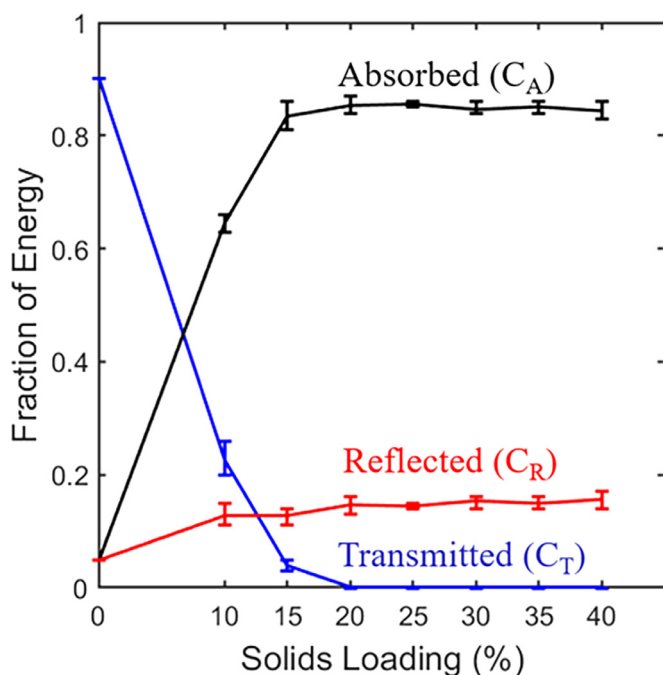
Fig. 9. The absorption, reflection and transmission coefficients for λ = 532 nm.

and 40 wt.% respectively. Since thermal diffusivity is dependent on thermal conductivity, this is consistent with studies showing micron aluminum particles in PVDF have a higher overall thermal conductivity than pure PVDF [53], as well as studies showing pressed nAl pellets have a higher thermal conductivity than porous pellets with air voids [54]. For the low solids loading samples, the particles that heat up are surrounded by the lower thermal diffusivity PVDF, and while a few individual particles may ignite, there is not enough heat transfer to see bulk ignition of the sample. The solids loading of 20–25 wt.% results in an ideal scenario of enough particles to absorb the energy, while the thermal diffusivity is still low enough to not see significant heat dissipation. At 40 wt.% nAl, the MIE would be expected to rise as the heat conducted away is dispersed throughout the matrix, keeping the average temperature lower. It is important to note that both 10 and 40 wt.% samples have larger confidence intervals compared to the rest of the samples (Fig. 6). The 10 wt.% samples showed a large amount of variation when tested. Additionally, the accuracy of the test drops rapidly as the distance between the sample and the flash bulb is decreased. At 40 wt.% the increased variation is attributed to defects within the samples such as porosity that is introduced.

Ignition delay for varying solids loadings of nAl shows a similar trend as MIE (Fig. 6(b)). Using photodiode data, the burn rate of the films was observed and the delay from the start of the flash to full combustion was found. An energy of 8 J/cm^2 was used to ensure ignition of all samples tested. At low solids loadings, there is a large delay before the films steadily burn. As the solids loading approaches stoichiometric, the ignition delay drops before rising again at higher solids loadings.

3.3. Nd: YAG laser ignition

Using the Nd: YAG fundamental and second harmonic frequencies (1064 nm and 532 nm), the effects of solids loading in nAl/PVDF films were studied using narrowband wavelengths as opposed to the broadband flash seen in the xenon flash lamp. Using the pulse burst mode, the laser was operated at a burst duration of 5 ms with a repetition rate of 100 kHz to simulate a similar temporal profile as the flash. Due to the 10 ns pulses, a large amount of

energy was delivered per pulse within the burst while still maintaining a relatively low overall energy profile for ignition purposes. The MIE was again found utilizing the Neyer sensitivity test for both wavelengths. These results were then compared to the flash MIE values (Fig. 7).

At 15 wt.% nAl and above, the laser ignition energy of nAl/PVDF samples were an order of magnitude lower than what was observed for flash ignition. Additionally, the MIE at all solids loading was nearly identical for both wavelengths, suggesting the nAl particles can equally absorb the light energy at both wavelengths. The MIE at 10 wt.% was significantly higher. This is because at lower energies, the samples would partially burn when hit with the laser energy, but not fully deflagrate. This was apparent from a hole surrounded by charred black material visible on the film after the laser was fired. The partial burning also supports the hypothesis that nAl is reacting at lower energies, but the flame is unable to spread throughout the films. While the samples did see an increase in MIE as the solids loading was increased past 25 wt.%, it was not as significant as the rise observed from flash ignition, indicating the defects or porosity have less of an effect for laser ignition. The ignition delay for 1064 nm showed little change as a result of solids loading but is again significantly smaller than flash ignition. In order to compare to the ignition delay from flash ignition, an energy of 8 J/cm^2 was used. Similarly to MIE, the ignition delay was nearly identical for 532 nm.

When comparing to the broadband flash, the stark decrease in MIE could be due to the discretized energy depositions of the laser energy and the thermal time constant of the nano-aluminum particles. The discretized laser energy deposition has a 1000:1 (10 μs:10 ns) ratio due to the 10 μs inter-pulse spacing. This means that for equivalent total energy deposition, the instantaneous laser energy is 1000 times larger than those from the flash. Assuming that the laser energy deposition energy is only thermal, as suggested by the independence of wavelength, then the reduction in MIE would only be caused by a faster time-averaged heating rate as seen by the particle. The faster heating rate from the cyclic laser heating would then be enabled by the inability of the nano aluminum particles to dissipate the thermal energy within the 10 μs between pulses. In other words, the faster heating rates are only possible for thermal time constants on the order of 10 μs for the nAl particles when embedded in a PVDF matrix. Thermal time constants of nAl particles have been reported to be 200 ns in shock tube studies with a Nusselt number of 2 [55]. For the shock tube study, convection dominates heat transfer which can be orders of magnitude larger than conduction. This decrease in heat dissipation should result in a proportional increase in time constant. Determination of the actual thermal time constant is outside the scope of this paper.

While the pulse burst setting is efficient for igniting the films by taking advantage of high intensity pulses, pulse burst lasers are still relatively new and uncommon. Therefore, a simplified laser heating setup would be more practical in real-world applications. The two lasers chosen for this study were a continuous wave laser with steady energy output, and a Q-switched laser with a large energy output in a single pulse. The laser was programmed to simulate a continuous wave laser with a 2 ms burst duration and inter-pulse spacing of 200 ns. The resulting laser had an energy deposition ratio of 20:1 (200ns:10 ns). Additionally, the burst was shortened to roughly 200 ns while maintaining the 200 ns inter-pulse spacing to simulate a single pulse Q-switched laser. Both of these settings were tested on 20 wt.% nAl/PVDF in an identical setup to previous laser ignition tests. Using the continuous wave setting, the 20 wt.% film was ignited at an energy as low as 0.6 J/cm^2, nearly the same energy as the pulse burst setting for a 5 ms burst. However, when the Q-switched setting was used, the film was not able to be ignited even at the maximum energy for that setting of
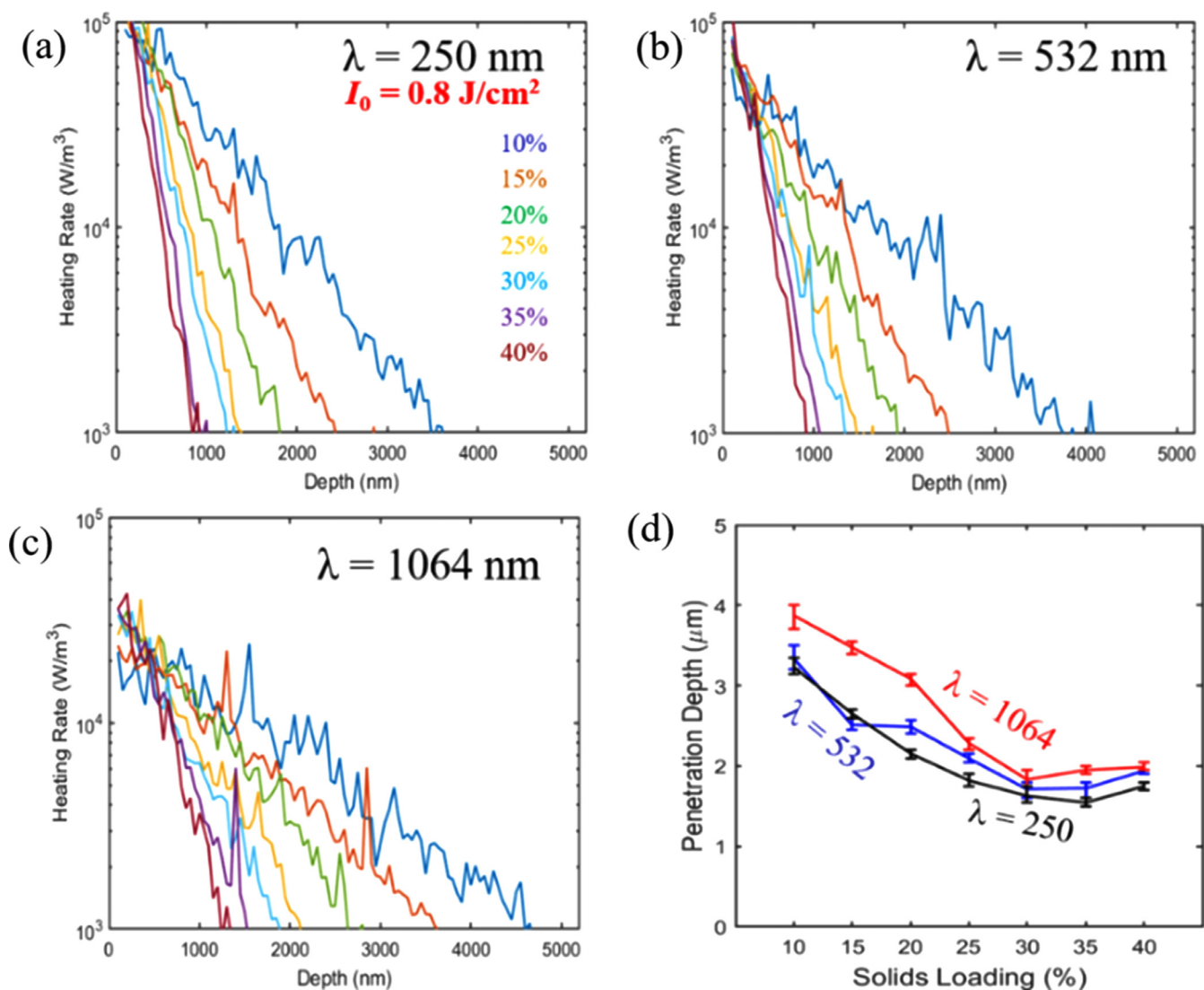
Fig. 10. Energy deposition in materials at different laser wavelengths. a) heating rate at 1064 nm b) heating rate at 532 nm, c) heating rate at 250 nm, d) Depth of heating penetration d_t as function of solids loading. The depth of penetration d_t is the thickness of the top layer of the sample in which the temperature reaches or exceeds the ignition temperature of Al $T = 630$ °C (900 K).

1.52 J/cm^2. The results of these tests can be seen in Fig. 8, and it is clear that the Q-switched setting ignites the film for the duration of the pulse but is quickly extinguished when the pulse ends. These findings indicate that there is a critical energy deposition ratio, equivalent to a heating rate, needed to achieve flame propagation and consequently full combustion.

3.4. Computational simulations

Calculations were carried out to analyze the heating in the nAl/PVDF samples caused by flash and laser excitation to better understand the response of nAl/PVDF. Depth of wave penetration, the plasmonic effect, and how solids loading affects ignition were investigated in this study. Fig. 9 contains the absorption, reflection, and transmission coefficients for each solids loading. Notably, the transmitted fraction of the wave is effectively zero once 20% solids loading is reached. Meaning all the incident energy from the wave is either reflected or absorbed. When energy is transmitted, it is around 20% of the incident energy, meaning for all samples analyzed most of the energy that drives ignition will be captured in the first 5 μm of the material. Most of the incident energy is absorbed by the material, with all but the 10% solids loadings having around 90% absorption of the wave. This trends helps to confirm the experimental observation that the MIE decreases as nAl solids loading is increased, specifically at around 20 wt.% nAl.

Figs. 10(a-c) show the energy deposited per unit volume per unit time (the energy deposition rate) at $t = 4.4$ μs at different depths into the material from the surface of exposure (top surface in Fig. 2). The intensity of the laser pulse is 0.8 J/cm^2. The three plots correspond to the three laser wavelengths, respectively. Overall, the deposition rate is highest at the surface and decreases with the depth into the material. At all wavelengths, the energy deposition rate decreases as the solids loading increases. This effect is especially significant at higher solids loadings. At higher solids loadings, energy deposition, and therefore heating, is limited to within a few microns of the top surface. The mechanism responsible for the trend is the generation of current in the nAl particles. Specifically, as the fraction of nAl particles increases, current flow increases near the surface. The consequence is twofold: one is increased Joule heating near the surface, and the other is the
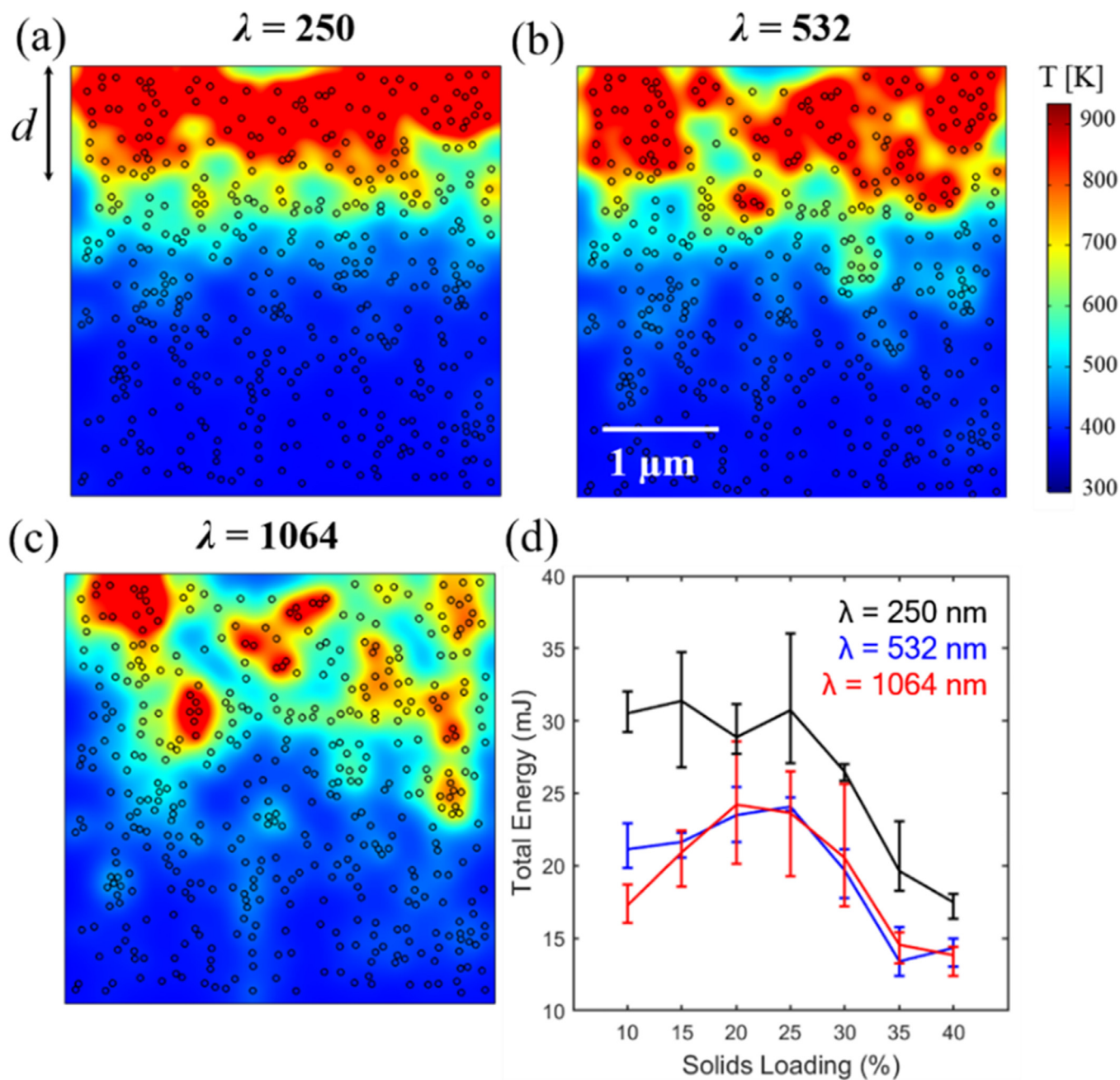
Fig. 11. a-c) Temperature Distributions of 10 wt.% solids loadings at $t = 343$ ns, $I_0 = 0.8$ J/cm^2, 250, 532, 1064 nm. d) Total energy deposited into the matrix vs solids loading for 250, 532, and 1064 nm.

increased shielding reflection that prevents further penetration of the EM wave deeper into the material, thereby resulting in overall lower heating.

To compare the heating distribution in the material, a measure of significant heating referred to as "depth of wave" or "heating penetration" is used. The thickness d_t is the top layer of the microstructure with average temperatures (along the horizontal direction) at or above the ignition temperature of Al (630 °C or 900 K) [56,57]. Fig. 10(d) compares this measure of the depth of penetration for different laser wavelengths, and we conclude that wave penetration decreases with increasing solids loading and higher wavelengths lead to deeper penetration.

The trends shown in Fig. 10 are due to the interactions between the microstructure and the EM waves. Specifically, the plasmonic effect is important when looking at these materials and their ig-

nition characteristics. The plasmonic effect results from enhanced particle-wave interactions (resonant oscillation of free electrons) at wavelengths much higher than the characteristic lengths of material heterogeneities. This effect enhances dissipation and heating [10] and has been studied for both nAl and nFe particles [9,10,43], leading to the conclusion that wavelength can be optimized to maximize heating for a given nanoparticle diameter [9]. The implication is that overall heating is affected by both the particle size, inter-particle distances (which depend on solids loading), and wavelength. To compare the effect of wavelength on heating, the temperature distributions in a sample with 10 wt.% solids loading at $t = 343$ ns are shown in Figs. 10(a-c). Overall, the trend is clear; at shorter wavelengths, heating is more concentrated near the top surface where exposure to the laser occurs and is more intense; at longer wavelengths, heating is more diffused and less intense.
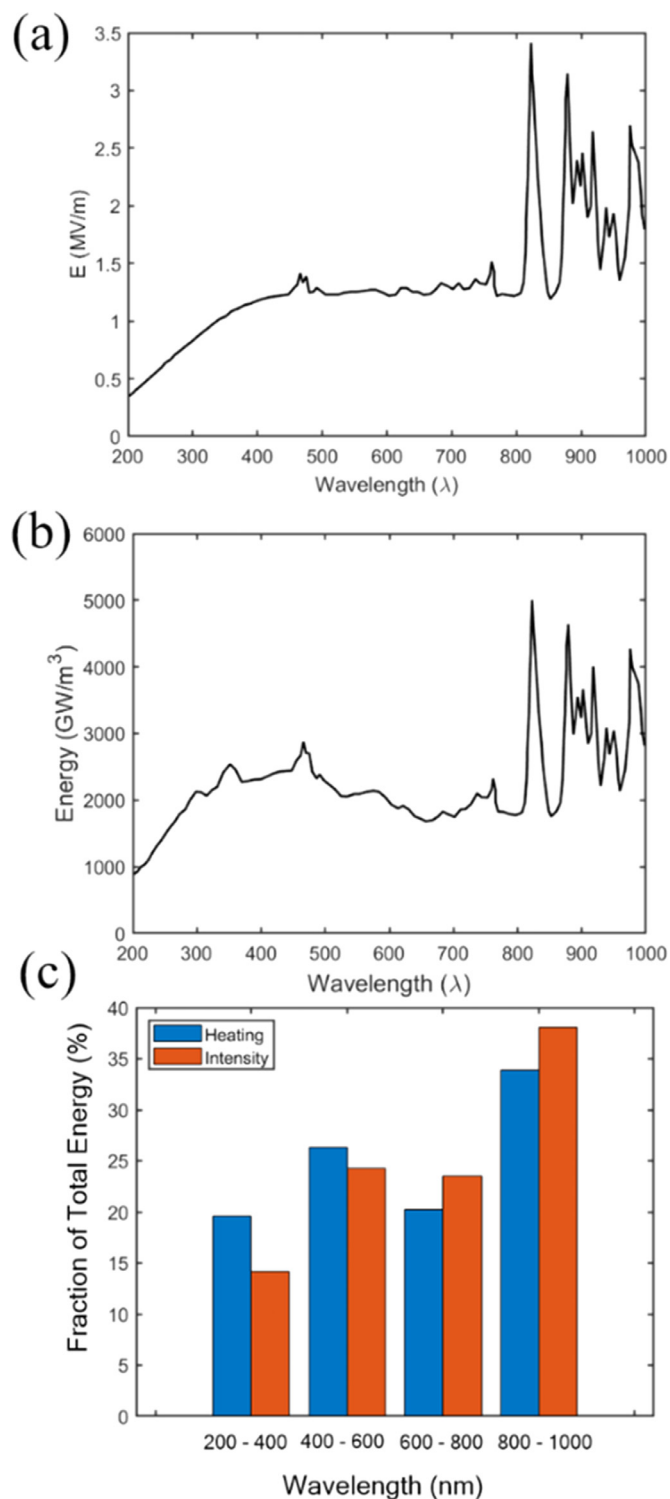
Fig. 12. a) Spectrum or relative intensities of different wavelengths of a xenon flash pulse, b) Energy deposited into a sample with 40 wt% solids loading as function of wavelength, c) contributions of different wavelength ranges to total energy deposited by flash pulse.

To quantify the difference, the total energy deposited (Q) into the layer of the material reaching the ignition temperature (d_t) is calculated using the Eq. 5. This allows us to focus on the part of the samples that is heated to the point of ignition. From Fig. 11, it can be seen that more heat is deposited in the top layer at 250 nm than at 1064 and 532 nm. This is primarily because the plasmonic

effect is stronger at the lowest wavelength for the length scales of the microstructures considered.

Since experiments are carried out at 1064 and 532 nm, we will focus our discussion on the results for the two wavelengths. The energy deposited is highest when the solids loading is near 20 to 25 wt.% and subsequently decreases as the solids loading increases towards 40 wt.%. Note that this trend is consistent with the inverse trend for MIE shown in Fig. 7. This is because of the underlying absorbency trend seen in Fig. 11(d). This absorbency trend reflects the outcome of the competing effects of wave penetration and reflection. Specifically, higher solids loading of nAl leads to higher current and more reflection, resulting in shallower penetration and lower energy dissipation. On the other hand, a higher current can lead to more Joule heating. The optimal energy deposition at ~ 20–25 wt.% solids loading also reflects the effects of thermal conduction which are explicitly accounted for in the analyses (see Eq. (3)).

Calculations are also carried out to study the heating due to a broadband energy source such as a xenon lamp. The objective is to simply outline which factor is more important in causing the heating behavior observed in experiments: wavelength or relative intensity of different wavelengths in the broadband pulse. To this purpose, a spectrum experimentally measured for xenon flash bulbs (see Fig. 11(a)) is used. The wavelength range of the spectrum is 200–1000 nm, as noted earlier. This profile has large intensity spikes in the infrared range (800–1000 nm) and relatively low intensities in the ultraviolet range (200–400 nm), see Fig. 12(a).

To compare the effects on heating of the different wavelengths in the spectrum, calculations are carried out for the microstructures at discrete single wavelengths between 200 and 1000 at an increment of 5 nm, therefore a total of 160 single-wavelength calculations are conducted, each at the corresponding relative intensity shown in Fig. 12(a). The resulting heating rate (energy deposited in the sample per unit time) as a function of wavelength is shown in Fig. 12(b). Note that the profiles in Figs. 12(a) and (b) are very similar, indicating that the relative contributions from different wavelengths are primarily determined by their relative intensities, therefore, the effect of wavelength is relatively minor. To further gain insight, the wavelengths were grouped into an ultraviolet range (200–400 nm), two intermediate ranges of 400–600 nm and 600–800 nm, and an infrared range (800–1000 nm). The total energy deposited by the flash pulse was obtained by integrating the energy deposition contributions from different wavelengths over the range studied. This allows the contribution of each of the wavelength ranges to the overall energy deposition to be evaluated. The result is shown in Fig. 12(c) for the solids loading of 40 wt.%. Note that the same trend is observed for other solids loadings.

Fig. 12(c) shows that there is an increase in heating from the 200–400 range as well as from the 400–600 range. This means that both of these ranges provide a larger amount of energy than would be expected if there were no wavelength dependency. These fractions include the effects of both relative intensities and wavelength, including the plasmonic effect which can be more pronounced here at the lower end of the wavelength spectrum (200–400 nm) [9]. This was seen in the 250 nm single wavelength laser heating results discussed earlier.

4. Conclusions

We have produced full density energetic films of nAl and PVDF that can be ignited by laser or broadband light excitation. Experiments were carried out using xenon broadband flash and a Nd:YAG laser, with ignition energies as low as 4.7 and 0.6 J/cm^2, respectively. These ignition energies represent the minimum energy fluence from the laser or flash source required for ignition probability of 50%. No significant difference in results between 1064 and

532 nm was found experimentally. Solids loading was found to be the dominating factor controlling minimum ignition energies, with the lowest energies observed at 20 to 25 wt.% nAl. This optimal solids loading reflects a balance between sufficient energy absorption and low overall thermal diffusivity of the sample to avoid pronounced heat loss away from hotspots. This trend was also observed for ignition delay of the nAl/PVDF films when flash ignited, but laser ignition showed a consistent ignition delay for the samples when tested at the same energy as the flash. More tests would need to be conducted to measure ignition delay at lower energies for laser ignition.

In addition to successful ignition with a pulse burst laser, we also showed that the films could be ignited in a continuous wave laser setting. In order to emulate the effects of more common lasers, the laser was programmed to resemble both a Q-switched laser with a high pulse energy and a relatively short pulse of 0.2 ms, as well as a continuous wave laser with a pulse duration of 2 ms. The films were only able achieve sustained combustion using the continuous wave mode, and at an ignition energy as low as 0.6 J/cm^2. Although the Q-switched mode created localized burning, the flame was quenched after the pulse, even at the highest energy setting.

Microstructure level computational simulations were conducted using COMSOL [48] to understand the heating mechanisms responsible for the laser and flash ignition. The results show that optimal energy absorption occurs at nAl particle fractions of ~20–25 wt.%, consistent with the experimental observation. This optimal solids loading level reflects a balance between the heat conduction, effects of wave penetration, wave reflection, and Joule heating. The analyses also show the effect of plasmonic resonant enhancement of the heating, which is most pronounced at lower wavelengths near 250 nm and less significant at the higher wavelengths of 1064 nm and 532 nm. Analysis of the broadband flash heating show that the plasmonic effect is pronounced at wavelengths from 200 to 400 nm and contributes to a significant portion of the total energy deposited. However, for the experiments performed, plasmonic effects are minimal. The relative intensities of different wavelengths in the flash spectrum dominate the wavelength contributions to the overall heating.

Declaration of Competing Interest

The authors declare that they have no known competing financial interests or personal relationships that could have appeared to influence the work reported in this paper.

Acknowledgments

Disclosure statement

The authors declare no conflict of interests.

Supplementary materials

Supplementary material associated with this article can be found, in the online version, at doi:10.1016/j.combustflame.2021.111570.

References

[1] G.L. Vonpragenau, Solid Rocket Motor Igniters, 1971.

[2] G. Bryan, G. Edwards, A Method for Predicting Ignition Energy Requirements for Practical Propellant Systems, White Oak, Maryland, 1955.

[3] P.M. Ajayan, M. Terrones, A. De la Guardia, V. Huc, N. Grobert, B.Q. Wei, H. Lezec, G. Ramanath, T.W. Ebbesen, Nanotubes in a flash - Ignition and reconstruction, Science (80 -.). 296 (2002) 705. https://doi.org/10.1126/science.296.5568.705.

[4] M.R. Manaa, A.R. Mitchell, P.G. Garza, P.F. Pagoria, B.E. Watkins, Flash ignition and initiation of explosives-nanotubes mixture, J. Am. Chem. Soc. 127 (2005) 13786–13787, doi:10.1021/ja0547127.

[5] G. Liu, D. Liu, J. Zhu, J. Wei, W. Cui, S. Li, Energy conversion and ignition of fluffy graphene by flash light„ Energy 144 (2018) 669–678, doi:10.1016/j.energy.2017.12.062.

[6] S.H. Tseng, N.H. Tai, W.K. Hsu, L.J. Chen, J.H. Wang, C.C. Chiu, C.Y. Lee, L.J. Chou, K.C. Leou, Ignition of carbon nanotubes using a photoflash, Carbon N. Y. 45 (2007) 958–964, doi:10.1016/j.carbon.2006.12.033.

[7] Y. Ohkura, P.M. Rao, X. Zheng, Flash ignition of Al nanoparticles: mechanism and applications, Combust. Flame. 158 (2011) 2544–2548, doi:10.1016/j.combustflame.2011.05.012.

[8] D. Liu, Y. Liu, G. Liu, Effects of carbon nanotubes additions on flash ignition characteristics of Fe and Al nanoparticles, fullerenes, nanotub., Carbon Nanostruct. 26 (2018) 168–174, doi:10.1080/1536383X.2017.1420062.

[9] X. Chong, N. Jiang, Z. Zhang, S. Roy, J.R. Gord, Plasmonic resonance-enhanced local photothermal energy deposition by aluminum nanoparticles, J. Nanoparticle Res. (2013) 15, doi:10.1007/s11051-013-1678-2.

[10] J.E. Abboud, X. Chong, M. Zhang, Z. Zhang, N. Jiang, S. Roy, J.R. Gord, Photothermally activated motion and ignition using aluminum nanoparticles, Appl. Phys. Lett. (2013) 102, doi:10.1063/1.4776660.

[11] Y.X. Liu, D. Liu, G.N. Liu, Energy conversion and ignition of iron nanoparticles by flash, Sci. China Technol. Sci. 60 (2017) 1878–1884, doi:10.1007/s11431-017-9144-6.

[12] Y. Jiang, S. Deng, S. Hong, J. Zhao, S. Huang, C.C. Wu, J.L. Gottfried, K.I. Nomura, Y. Li, S. Tiwari, R.K. Kalia, P. Vashishta, A. Nakano, X. Zheng, Energetic performance of optically activated aluminum/graphene oxide composites, ACS Nano 12 (2018) 11366–11375, doi:10.1021/acsnano.8b06217.

[13] F. Yang, Y. Zhang, X. Yang, M. Zhong, Z. Yi, X. Liu, X. Kang, J. Luo, J. Li, C.Y. Wang, H.B. Zhao, Z.B. Fu, Y.J. Tang, Enhanced photothermal effect in ultralow-density carbon aerogels with microporous structures for facile optical ignition applications, ACS Appl. Mater. Interfaces. 11 (2019) 7250–7260, doi:10.1021/acsami.8b17803.

[14] R.J. Seymour, Fiber Optics Ignition 3 (258) (1966) 910.

[15] L. DeLuca, L.H. Caveny, T.J. Ohlemiller, M. Summerfield, Radiative ignition of double-base propellants. I. Some formulation effects, AIAA J 14 (1976) 940–946, doi:10.2514/3.7167.

[16] M. Nakano, H. Koizumi, M. Watanabe, Y. Arakawa, A laser ignition microthruster for microspacecraft propulsion, Trans. Japan Soc. Aeronaut. Sp. Sci. Sp. Technol. Japan. 7 (2009) Pb_7-Pb_9, doi:10.2322/tstj.7.pb_7.

[17] V.A. Arkhipov, A.G. Korotkikh, The influence of aluminum powder dispersity on composite solid propellants ignitability by laser radiation, Combust. Flame. 159 (2012) 409–415, doi:10.1016/j.combustflame.2011.06.020.

[18] S.R. Ahmad, M. Cartwright, Laser Ignition of Energetic Materials, John Wiley & Sons, 2014.

[19] N.N. De, N.R. Cummock, I.E. Gunduz, B.C. Tappan, S.F. Son, Photoflash and laser ignition of select high-nitrogen materials, Combust. Flame. 167 (2016) 207–217, doi:10.1016/j.combustflame.2016.02.011.

[20] P. Gillard, L. Courty, S. De Persis, J.F. Lagrange, C. Boulnois, I. Gökalp, Combustion properties of a low-vulnerability propellant: an experimental and theoretical study using laser ignition, J. Energ. Mater. 36 (2018) 362–374, doi:10.1080/07370652.2018.1439126.

[21] L. Courty, J.F. Lagrange, P. Gillard, C. Boulnois, Laser ignition of a low vulnerability propellant based on nitrocellulose: effects of Ar and N2 surrounding atmospheres, Propellants, Explos. Pyrotech. 43 (2018) 986–991, doi:10.1002/prep.201800087.

[22] D.M. Dyrda, F.S. Mechentel, B.J. Cantwell, A.C. Karp, J. Rabinovitch, E.T. Jens, Diode laser ignition of a poly(methyl methacrylate) and gaseous oxygen hybrid motor, J. Propuls. Power. (2020) 1–10, doi:10.2514/1.b37832.

[23] N. Williams, United States Patent: 5861366 United States Patent : 5861366, 1977, pp. 1–29. New York.

[24] M. Harayama, T. Saito, A. Iwama, Ignition of composite solid propellant at subatmospheric pressures, Combust. Flame. 52 (1983) 81–89, doi:10.1016/0010-2180(83)90122-0.

[25] L. De Yong, F. Lui, Radiative ignition of pyrotechnics: effect of wavelength on ignition threshold, Propellants, Explos. Pyrotech. 23 (1998) 328–332 6<328::AID-PREP328>3.0.CO;2-H, doi:10.1002/(SICI)1521-4087(199812)23.

[26] C. Zanotti, P. Giuliani, Composite propellant ignition and extinction by CO$_2$ laser at subatmospheric pressure, Propellants, Explos. Pyrotech. 23 (1998) 254–259 AID−PREP254>3.0.CO;2-3, doi:10.1002/(SICI)1521-4087(199811)<254.

[27] S. Rafi Ahmad, D.A. Russell, C.J. Leach, Studies into laser ignition of unconfined propellants, Propellants, Explos. Pyrotech. 26 (2001) 235–245 AID−PREP235>3.0.CO;2-9, doi:10.1002/1521-4087(200112)26:5<235.

[28] J.W. Weber, M.Q. Brewster, K.C. Tang, Radiative ignition and extinction dynamics of energetic solids, J. Thermophys. Heat Transf. 19 (2005) 257–265, doi:10.2514/1.12072.

[29] J. Cain, M.Q. Brewster, Radiative ignition of fine-ammonium perchlorate com-

posite propellants, Propellants, Explos. Pyrotech. 31 (2006) 278–284, doi:10.1002/prep.200600037.

[30] A. Kakami, R. Hiyamizu, K. Shuzenji, T. Tachibana, Laser-assisted combustion of solid propellant at low pressures, J. Propuls. Power. 24 (2008) 1355–1360, doi:10.2514/1.36458.

[31] X. Huang, Y. Yang, F. Hou, S. Li, Z. Qin, F. Zhao, Laser-induced ignition and combustion of Al−Mg alloy powder prepared by melt atomization, Propellants, Explos. Pyrotech. 45 (2020) 1645–1653, doi:10.1002/prep.202000058.

[32] F. Hou, S. Li, Y. Wang, X. Huang, Laser-induced ignition and combustion of individual aluminum particles below 10 μm by microscopic high-speed cinematography, Processes 8 (2020), doi:10.3390/pr8030280.

[33] X. Jin, S. Li, Y. Yang, X. Huang, Comparison on laser ignition and combustion characteristics of nano- and micron-sized aluminum, Combust. Sci. Technol. 193 (2021) 341–353, doi:10.1080/00102202.2020.1800659.

[34] F. Al-Ramadhan, I. Haq, M. Chaudhri, Low-energy laser ignition of magnesium-Teflon- Viton compositions, (1993).

[35] J.J. Granier, M.L. Pantoya, Laser ignition of nanocomposite thermites, Combust. Flame. 138 (2004) 373–383, doi:10.1016/j.combustflame.2004.05.006.

[36] J.H. Kim, M.H. Cho, K.J. Kim, S.H. Kim, Laser ignition and controlled explosion of nanoenergetic materials: the role of multi-walled carbon nanotubes, Carbon N. Y. 118 (2017) 268–277, doi:10.1016/j.carbon.2017.03.050.

[37] A.R. Demko, C. Dillier, T. Sammet, E.L. Petersen, D.L. Reid, S. Seal, Ignition delay times of composite solid propellants using novel nano-additive catalysts, J. Propuls. Power. 34 (2018) 1285–1296, doi:10.2514/1.B36802.

[38] E. Forat, V. Medvedev, V. Tsipilev, A. Yakovlev, The influence of aluminum and ammonium perchlorate dispersion on characteristics of the laser ignition, (2018) 186–188.

[39] S. Churchyard, X. Fang, R. Vrcelj, Laser ignitibility of energetic crystals doped with gold nanoparticles, Opt. Laser Technol. 113 (2019) 281–288, doi:10.1016/j.optlastec.2018.12.021.

[40] Y. Ohkura, J.M. Weisse, L. Cai, X. Zheng, Flash ignition of freestanding porous silicon films: effects of film thickness and porosity, Nano Lett 13 (2013) 5528–5533, doi:10.1021/nl403114g.

[41] T.R. Sippel, S.F. Son, L.J. Groven, Modifying aluminum reactivity with poly(carbon monofluoride) via mechanical activation, Propellants, Explos. Pyrotech. 38 (2013) 321–326, doi:10.1002/prep.201200202.

[42] Y. Ohkura, P.M. Rao, I.Sun Cho, X. Zheng, Reducing minimum flash ignition energy of Al microparticles by addition of WO_3 nanoparticles, Appl. Phys. Lett. (2013) 102, doi:10.1063/1.4790152.

[43] X. Chong, J. Abboud, Z. Zhang, Plasmonics resonance enhanced active photothermal effects of aluminum and iron nanoparticles, J Nanosci Nanotechnol (2015) 15, doi:10.1166/jnn.2015.9698.

[44] R. Malureanu, A. Lavrinenko, Ultra-thin films for plasmonics: a technology overview, Nanotechnol. Rev. 4 (2015) 259–275, doi:10.1515/ntrev-2015-0021.

[45] S. Salaeh, P. Cassagnau, G. Boiteux, S. Wießner, C. Nakason, Thermoplastic vulcanizates based on poly(vinylidene fluoride)/Epoxidized natural rubber blends: effects of phenolic resin dosage and blend ratio, Mater. Chem. Phys. 219 (2018) 222–232, doi:10.1016/j.matchemphys.2018.08.029.

[46] M.E. Smyser, K.A. Rahman, M.N. Slipchenko, S. Roy, T.R. Meyer, Compact burst-mode Nd:YAG laser for kHz–MHz bandwidth velocity and species measurements, Opt. Lett. 43 (2018) 735, doi:10.1364/ol.43.000735.

[47] B.T. Neyer, More Efficient Sensitivity Testing, Miamisburg, OH, USA, 1989.

[48] COMSOL Multiphysics® v. 5.4. www.comsol.com COMSOL AB, Stockholm, Sweden., (n.d.).

[49] J. Sun, M. Huang, J. Peng, W. Niu, L. Zhang, The simulation of the frequency-dependent effective permittivity for composite materials, Proc. 9th Int. Symp. Antennas, Propag. EM Theory (2010), pp. 701–704, doi:10.1109/ISAPE.2010.5696563.

[50] W. Bäumler, E. Vural, M. Landthaler, F. Muzzi, G. Shafirstein, The effects of intense pulsed light (IPL) on blood vessels investigated by mathematical modeling, Lasers Surg. Med. 39 (2007) 132–139, doi:10.1002/lsm.20408.

[51] V.E. Ferry, A. Polman, H.A. Atwater, Modeling light trapping in nanostructured solar cells, ACS Nano 5 (2011) 10055–10064, doi:10.1021/nn203906t.

[52] Q. Chen, H. Qi, Y.T. Ren, J.P. Sun, L.M. Ruan, Optical properties of truncated Au nanocages with different size and shape, AIP Adv 7 (2017), doi:10.1063/1.4990409.

[53] W. Zhou, J. Zuo, W. Ren, Thermal conductivity and dielectric properties of Al/PVDF composites, Compos. Part A Appl. Sci. Manuf. 43 (2012) 658–664, doi:10.1016/j.compositesa.2011.11.024.

[54] S.C. Stacy, X. Zhang, M. Pantoya, B. Weeks, The effects of density on thermal conductivity and absorption coefficient for consolidated aluminum nanoparticles, Int. J. Heat Mass Transf. 73 (2014) 595–599, doi:10.1016/j.ijheatmasstransfer.2014.02.050.

[55] V.I. Levitas, Burn time of aluminum nanoparticles: strong effect of the heating rate and melt-dispersion mechanism, Combust. Flame. 156 (2009) 543–546, doi:10.1016/j.combustflame.2008.11.006.

[56] M.A. Trunov, S.M. Umbrajkar, M. Schoenitz, J.T. Mang, E.L. Dreizin, Oxidation and melting of aluminum nanopowders, J. Phys. Chem. B. 110 (2006) 13094–13099, doi:10.1021/jp0614188.

[57] R.A. Yetter, G.A. Risha, S.F. Son, Metal particle combustion and nanotechnology, Proc. Combust. Inst. 32 II (2009) 1819–1838, doi:10.1016/j.proci.2008.08.013.